ADVANCED OPTICAL MATERIALS
www.advopticalmat.de

Metallized Gratings Enable Color Effects and Floating Screen Films by First-Order Diffraction

Fabian Lütolf, Martin Stalder, and Olivier J. F. Martin*

A new concept for generating visual effects with metallized gratings is introduced. Shadow evaporation of aluminum onto dielectric gratings is shown to produce strongly asymmetric color effects. Zero-order effects are combined with ±first-order transmission in the present structures to generate not only polarization but also orientation-dependent colors. We show that a wide palette of colors can be obtained by simply scaling the parameters of the dielectric base grating. The present approach therefore enables the fabrication of entire asymmetric images in a two-step process. Additionally, a floating screen film is created by placing the grating at an increased distance to the light source. The present structures could find applications as security or decorative elements and are well suited for mass production using high-throughput techniques such as roll-to-roll fabrication.

1. Introduction

Nanostructures occurring naturally on plants or animals, such as the lotus or various butterflies, have inspired research into developing diverse materials and effects based on similar features.[1–6] Physical color effects, such as those found for example on the wings of the Morpho butterfly are often caused by complicated periodic structures, which can be quite difficult to produce with the available technologies.[7] Gratings, on the other hand, are also a source of naturally occurring colors – for instance, on the less famous Troides magellanus[8] – but they are much easier to produce artificially.[9,10] Different kinds of gratings have therefore been used for several decades to produce physical colors, especially for applications in the field of security.[11,12] An appealing feature of such physical colors is their tunability[13] and the fact that they are less prone to environmental influences, such as photobleaching, than for instance their chemical counterparts.

The interest in creating colors with gratings has more recently resurged when Ebbesen et al. described extraordinary optical transmission and attributed this effect to plasmon resonances supported by a periodic array of metallic nanoholes.[14] Although such effects had already been heavily discussed on periodic 2D structures, subsequent research transferred the findings to 1D gratings in different configurations.[15–20] Apart from the utilization of plasmonic color effects for security applications,[21] the possibility of generating colors with 1D metal gratings that do not support plasmon resonance has also been described by different authors.[22–24]

Diffractive systems have been shown to support tunable colors in zero-order transmission (*T*0) as well as higher order modes. The former are for instance enabled by grating resonances and redistribution of light into higher diffraction orders invisible to the observer.[11] The latter are often based on stretchable substrates and exhibit an elongation-dependent color at a given angle.[25,26] In contrast to this previous work, we do not only use one diffraction order, on the contrary we combine colored zero-order and first-order transmission (*T*1), which increases the number and diversity of the visual color effects available from one single sample.

Various classes of asymmetric gratings have been reported,[27–29] but to the best of our knowledge these have never been optimized for color effects. To this end, we introduce a different geometry to what is normally used in metal-evaporated gratings: by increasing the evaporation angle with respect to the surface normal, the bottom of the grating remains uncovered while L-shaped disconnected metal wires are formed, instead of the Z-shaped ones reported earlier.[22] In addition to the well-known polarization dependence of the optical transmission through such gratings, this approach also induces an orientational dependence of the optical appearance. Such asymmetric color effects are of great interest for security applications and their possible utilization will be illustrated by presenting a structure that enables floating screen films. This eye-catching effect could not only find applications in security, but for example also in decoration or marketing by combining it with light-emitting devices, such as mobile phones or tablets (could be integrated into showcases or the transparent wrapping they are delivered in).

2. Results and Discussion

2.1. Diffraction Theory

For the color effects reported in the present work, the zero-order transmittance (*T*0) as well as the ±1st-order transmittances

F. Lütolf, Dr. M. Stalder
CSEM Muttenz, Tramstrasse 99
Muttenz 4132, Switzerland
E-mail: martin.stalder@csem.ch
Prof. O. J. F. Martin
Nanophotonics and Metrology Laboratory (NAM)
Swiss Federal Institute of Technology Lausanne (EPFL)
Lausanne 1015, Switzerland

DOI: 10.1002/adom.201500305

($T1/T-1$) are important. A very useful equation to describe the behavior of higher orders is the well-known grating equation for classical diffraction. When it is solved for the output angle θ_m^T of a given transmitted order m, it allows to predict the angles at which diffracted light of a given wavelength λ becomes visible:

$$\theta_m^T = \sin^{-1}\left(\frac{n_1 * \sin(\theta_i) + m * \frac{\lambda}{\Lambda}}{n_2}\right) \quad (1)$$

The key parameters here are the refractive indices of the superstrate (n_1) and substrate (n_2) as well as the angle of incidence θ_i and the grating period Λ. As asymmetric gratings are considered in the present article, the sign of θ_i is important and must be chosen as shown in **Figure 1**b, following grating physics, as defined for example by Palmer and Loewen.[30] Throughout the rest of this article, the color code shown on this image will be kept for $T0$, but not for the ±1st order. Indeed, the problem when labeling the diffraction orders according to the general convention is that optical paths linked through reciprocity do not hold the same name when coming from either side of the grating surface. It has been shown that $T1$, as it is labeled in Figure 1b, tends to show a very high diffraction efficiency of up to 55% for transverse electric (TE) polarized light[31] (see Figure S1 in the Supporting Information). On the other hand, the opposite is true for $T-1$, which is well below 10% at any angle and wavelength. The reciprocal rays are of course diffracted with the same efficiency, but the naming of their order should be switched. Throughout the rest of this article, we will therefore refer to the orders as the "high-efficiency order", $T1_{hi}$, and the "low-efficiency order", $T1_{low}$, as depicted in Figure 1c.

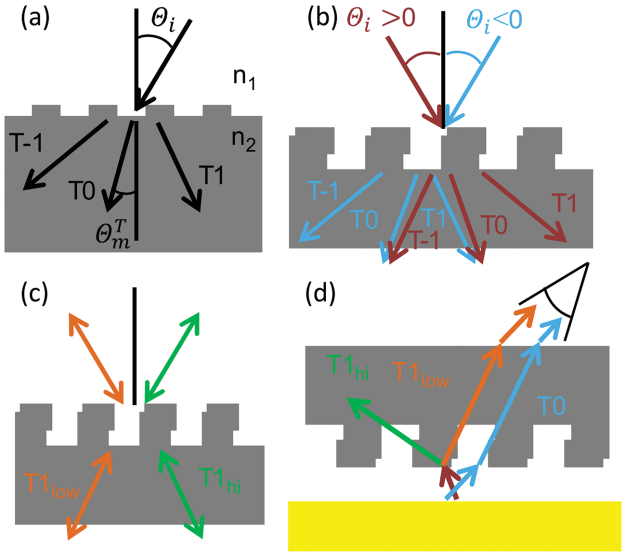

Figure 1. a) Schematic showing the propagation direction of 0 and ±1st diffracted orders inside a medium with $n_2 > n_1$ after having passed through an arbitrary grating interface. b) Illustration of the choice of sign and color coding for the incident angle with respect to the metallization. The resulting diffracted orders and how they combine is also shown. c) The reciprocity of the diffracted orders and their labeling based on the transmitted intensities. d) Visualization of how $T-1$ and $T0$, coming from different parts of an extended light source, can form a mixed color that is visible to the observer.

One important feature already is visible from Figure 1b: $T0$ stemming from light with a negative angle of incidence ($\theta_i < 0$, blue arrows) can be refracted to the same angle as light diffracted from a positive angle ($\theta_i > 0$, red arrows $T-1$). This is an important mechanism when considering extended light sources, such as a display or other flat-panel light sources that radiate into a large solid angle. To illustrate this fact, let us consider a numerical example for green light (530 nm) and a grating with a Λ = 440 nm period. We further assume that we want green $T-1$ light to become visible at $\theta_{-1}^T = -40°$ after passing through the sample together with the $T0$ light, as sketched in Figure 1d. Snell's law indicates that the refracted $T0$ light will travel at an angle of approx. –25° inside the glass. Considering a ray coming from the air side (red arrow in Figure 1d), we set $n_1 = 1$, $n_2 = 1.5$, $\Lambda = 440$ nm, $\lambda = 530$ nm and $m = -1$. Equation (1) yields $\theta_{-1}^T = -25°$ for an angle of incidence θ_i around 35°, which is what we searched for. The same can be done for any other wavelength in order to find all the incoming light that is diffracted to $\theta_{-1}^T = -40°$ (alternatively, we could of course have considered the reciprocal ray incident at $\theta_i = -40°$ from the back side). At a $\theta_m^T = -40°$ angle of observation, the T0 light is therefore visible simultaneously as light that is diffracted into $T-1$ and impinges onto the grating surface at different angles (and hence comes from different parts of the light source).

2.2. Color Effects

The best known transmission color effects reported in the literature are zero-order transmission effects and hence this geometry will also be investigated first for the present structures. As mentioned, we are interested in color effects that are asymmetric with respect to rotation or tilt of the structure and we therefore require seeing color effects at an angle. For this purpose, a grating with a Λ = 440 nm period and t = 250 nm depth was evaporated with D = 20 nm Al at an angle $\alpha > 60°$ and subsequently spectrally characterized for both polarizations (**Figure 2** shows the fabrication procedure as well as the definition of polarizations) at angles between –60° and 60° (**Figure 3**).

The spectra show several distinct features for the two polarizations, which results in a strong color difference between them that is visible to the naked eye (see photos in the inset of Figure 3). The spectral features of transverse magnetic (TM) polarized light are mainly located outside of the visible wavelength range (resulting in a greyish color) as can be seen in Figure 3a, whereas the opposite is true for TE polarized light, see Figure 3b. The difference between the positive and negative angles is very strong for TE polarized light, with a drop from around 55% of green/orange light transmittance at 20° to around 5% at –40°. Figure 3c illustrates this further: by dividing the transmittance spectra recorded at $+\theta_0^T$ by those recorded at $-\theta_0^T$, the resulting "asymmetry ratio" reached a value of 9 for visible wavelengths. The structure therefore appears 9 times more transparent for certain wavelengths when looking at it from positive angles than when looking from the corresponding negative angles.

Adv. Optical Mater. **2015**,
DOI: 10.1002/adom.201500305

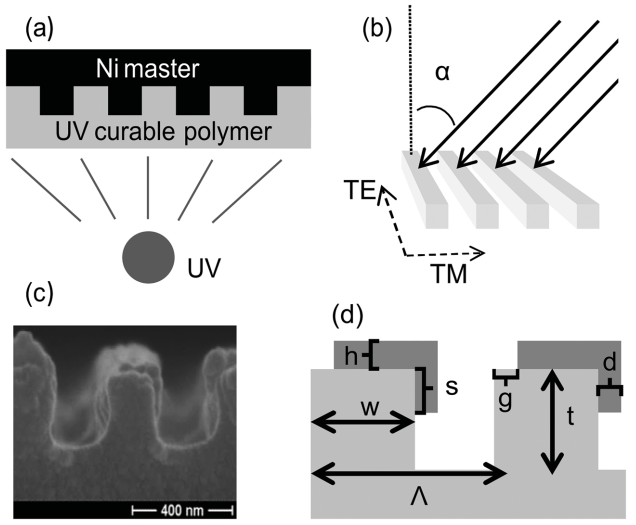

Figure 2. a) A subwavelength grating is cast in UV curable resin from a nickel shim; b) a layer of Al is evaporated on top of the replicated structure at an angle α; c) SEM image of the resulting structure; d) the simulation model deduced from the SEM image in (c) and the different parameters used in the simulations.

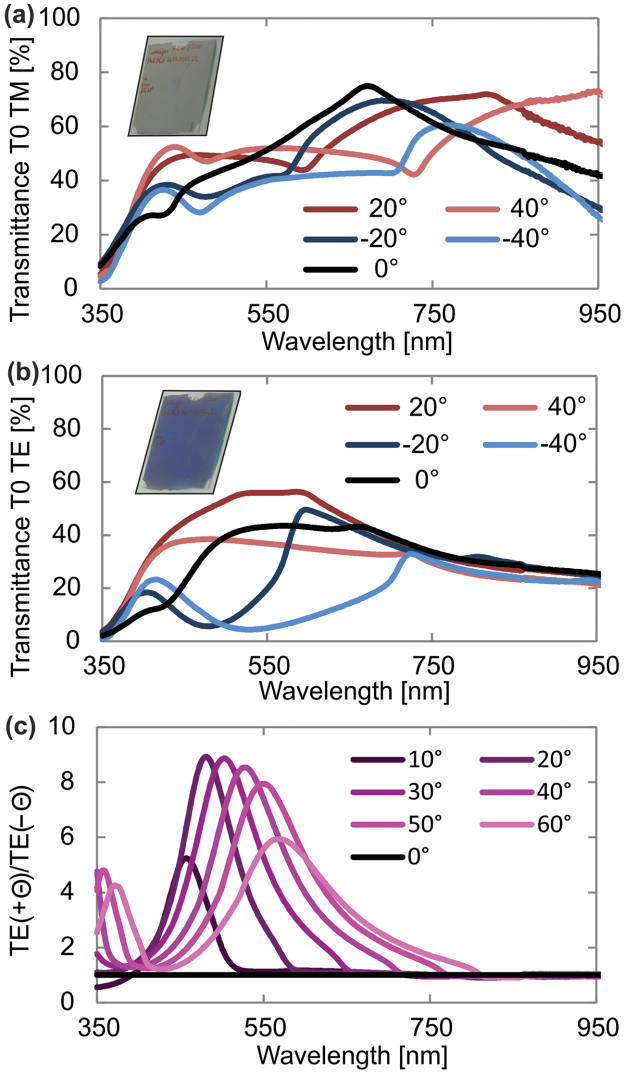

Figure 3. Zero-order transmittance spectra of a) TM-polarized light and b) TE-polarized light, measured on a 440-nm period grating with a layer of Al evaporated at $\alpha > 60°$. The insets show photos of the measured sample under accordingly polarized white-light illumination at an angle of $\theta^{T} = -40°$. The "asymmetry ratio" shown in (c) is defined by the transmittance of TE-polarized light at $+\theta_i$ divided by the transmittance of TE-polarized light at $-\theta_i$ for each wavelength.

It might appear obvious when simply considering the geometry that more light is reflected/absorbed when the ray is incident to the metallized side of the structure; however, this is not the correct explanation for this asymmetric response. As mentioned, the thin metal layer enables a very high $T1$ diffraction efficiency at any angle, reaching a peak at the wavelength around the Wood–Rayleigh anomaly. The anomaly occurs where the first reflected orders ($R\pm1$) vanish ($\theta_{\pm1}^{R} = 90°$), which is at $\lambda = \Lambda = 440$ nm for the sample under study at perpendicular air incidence. When tilting the grating, the $T1$ peak moves either into the UV (for $\theta_i > 0$) or into the visible (for $\theta_i < 0$). The large dip in $T0$ at negative angles is caused by exactly this redistribution of light into the higher order mode. The calculated $T1$ and $T-1$ efficiencies can be found in Figure S1 (Supporting Information). The graphs for $T0$ and $T1$ clearly complement each other at visible wavelengths for a –40° angle of incidence, which verifies the above claim. Note that the $T-1$ diffraction, which occurs at visible wavelengths for positive angles of incidence, is very inefficient and hence causes no modulation of the $T0$ spectrum.

Also visible in the TE spectra is the increasing reflection at steeper angles, reducing the overall transmittance for positive and negative angles (due to the reciprocity). Towards the infrared part of the spectrum, the metallized grating starts to behave like a wire grid polarizer, resulting in a high TE reflectance and high TM transmittance. It is finally worth mentioning that for TE polarized light, which shows a much stronger coloring in the present study, no surface plasmon resonances are excited.[32] The attained colors hence only rely on the diffractive properties and grating resonances, as is also the case in photonic crystals.[33]

Numerical simulations were performed using the geometry measured from the scanning electron microscopy (SEM) image (Figure 2c) of the grating. The simulated $T0$ data (violet line in **Figure 4**) fitted the measurements (dashed line) very well for the 440-nm period sample illuminated at $\theta_i = -40°$ (apart from for wavelengths below 470 nm, where the UV-curable polymer starts to absorb). The design parameters for the structures were the period Λ, the depth t, the ridge width w, the evaporation angle α, and the metallization thickness D. We limited ourselves to roll-to-roll compatible gratings with aspect ratios (structure height divided by structure depth, w/t) well below 2. For the 440-nm period grating, we therefore chose a maximal depth of 250 nm and a minimal ridge width $w = 0.3\Lambda$. Note that without these restrictions, deeper gratings could help to increase the diffraction efficiency and lowering the ridge widths would enhance the transmittance. As these are two of the key properties of our structures, however, the performance could further be improved by optimizing these features. The

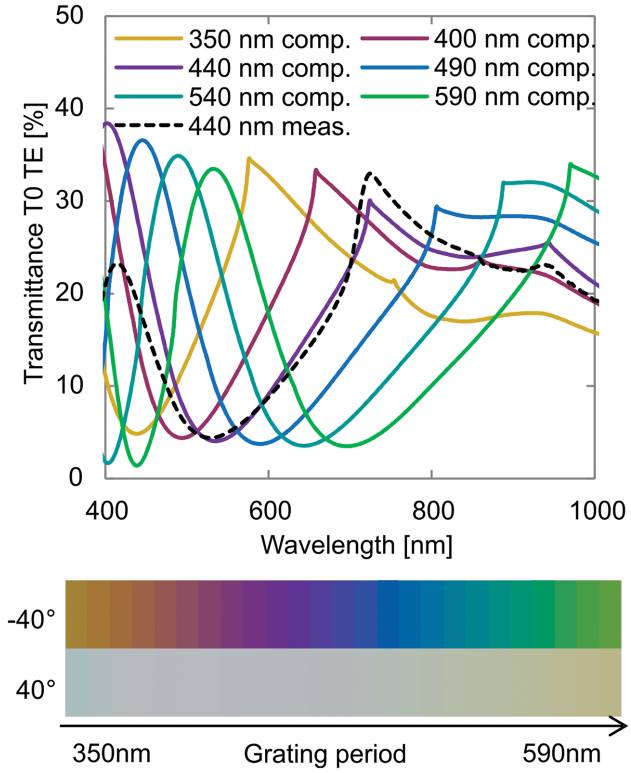

Figure 4. Computed zero-order transmittances at –40° TE polarized incidence for gratings with different periods (colored lines). The measured 440-nm period grating (dashed line) served as a basis and the corresponding model was equally scaled in period and depth for the whole series. The metallization parameters, such as the evaporation angle and thickness, were kept constant for the simulations. The resulting colors for $\theta_i = \pm 40°$ incidence of TE-polarized daylight are presented for periods between 350 nm and 590 nm. Note that the coloring of the spectral curves roughly corresponds to their computed perception.

evaporation angle was kept above 60° to make sure that only the ridges were coated. Coating the grating bottom would result in Z–shaped wires, for which the transmittance quickly deteriorates when increasing the viewing angle.[22] The metal thickness influences both $T0$ and $T1$ as shown in Figure S2 in the Supporting Information: Thicker metallization helps to increase the first-order efficiency, but unsurprisingly lowers the zero-order peak transmittance. 20 nm of aluminum seemed to be an optimal compromise between a high $T1$ efficiency (also resulting in strong $T0$ modulation) and a sufficiently high peak transmittance. Thinner metallization reduces the spectral modulation of the zero-order transmittance, whereas thicker metal layers mainly decrease the overall transmittance in $T0$. The expected colors for a metal thickness of 10 nm, 20 nm, and 30 nm are also shown in Figure S2. We saw that 10 nm of aluminum resulted in a lower saturation than 20 nm, whereas a 30-nm metal layer mainly produced a darker, slightly more reddish color. We therefore chose to go ahead with 20 nm of metal.

By increasing the period and depth of the base grating by the same factor (and thus keeping the aspect ratio constant), the $T0$ maxima situated at around λ = 420 nm and λ = 730 nm for the Λ = 440 nm period grating could be shifted to a longer or shorter wavelength (Figure 4). This can be well understood as both maxima are close to the Wood–Rayleigh anomaly (vanishing R–1 and R1 orders respectively; they are at different positions for oblique angles of incidence), which strongly depend on the period. The shape and height of the peaks are thus almost preserved. The period dependence of the spectral features has recently also been described for, for instance, photonic crystals[33] and allows very accurate control of the visible color. The colors computed for a ±40° viewing angle under daylight illumination are shown in Figure 4. With this palette of colors available it is straightforward to create colorful images at $\theta_i < 0$ that are hardly visible at $\theta_i > 0$ (only grey/brownish colors are observed in the latter case). Note that only TE-polarized zero-order transmittance is considered. This corresponds either to illumination with a very distant or collimated light source (such as, e.g., the sunlight) or the configuration in Figure 1d, where $T1_{low}$ can be neglected. It also requires the addition of a simple polarization filter, which is commercially available in large quantities at low prices.

It is worth emphasizing that the metallization parameters (thickness and evaporation angle) are the same for all the simulations in Figure 4. It is therefore possible to generate all of the above colors on one sample by using a single replication step (using a master consisting of gratings with different periods and depths) followed by one evaporation step. This color generation method is easier to implement in high-throughput systems than for example the electrical tuning of diffractive structures reported elsewhere.[34]

In order to illustrate how the achieved zero-order colors compare to other systems, the computed xy data for θ_i = –40° (grey) as well as θ_i = 40° angle of incidence (black) are plotted in the chromaticity diagram (**Figure 5**). All the colors enclosed by those curves are available through fabrication (e.g., through pixelation). We can immediately confirm that a variety of colors are perceivable at a viewing angle θ_i = –40°, whereas only a narrow range is available at 40°. By comparing our colors at –40° to the standard red–green–blue gamut (sRGB colors, available on

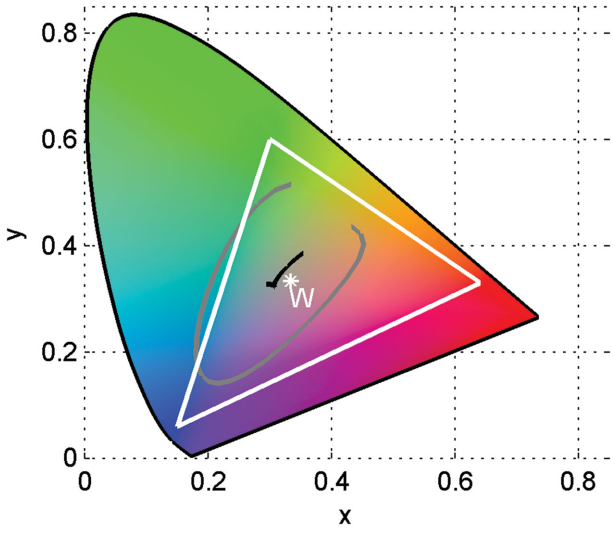

Figure 5. Chromaticity diagram displaying color data from computations in TE polarization on gratings scaled between 350 nm and 590 nm period (grey: –40°, black: 40° angle of view), the sRGB gamut (white triangle), and the white/color neutrality point (white asterisk labeled "W")

Adv. Optical Mater. **2015**,
DOI: 10.1002/adom.201500305

a standard LCD screen, white triangle in Figure 5), we see that our blue and green color availability is close to or even better than sRGB, but strong red hues are problematic. By removing some constraints (e.g., a constant evaporation parameter), further improvements should be possible, but such refinements go beyond the scope of the present report.

We experimentally show how a single evaporation can create two completely different colors on the same sample by patterning gratings with Λ = 440 nm and 350 nm periods into a "CSEM" shape and subsequently evaporating a 20-nm Al layer on top at an angle $\alpha > 60°$. The two gratings are predicted to show purple and orange colors, respectively, in zero-order transmission at a viewing angle of –40°, which was confirmed by our experiments (**Figure 6**). As established earlier, $T0$ accounts for the color visible in the orientation shown in Figure 1d and the top left photo in Figure 6 corresponds to this exact orientation. Rotating or flipping the device as indicated by the arrows will result in a well visible color change, leading to a 4-fold asymmetry. This switching happens due to the previously discussed mixing of $T0$ with either $T1_{hi}$ or $T1_{low}$ as sketched in Figure 6. The high, asymmetric diffraction efficiency here serves the double purpose of removing light from $T0$ as well as becoming directly visible to the observer in two of the possible configurations.

It is worth noting that the simulated colors for a 40° viewing angle matches the bottom right image where $T0$ is mixed with $T1_{low}$. The contrast between the two gratings is very low, as expected, and the CSEM logo is almost invisible apart from the white outline, which stems from the height difference between the two gratings and could be avoided by using a more sophisticated grating master. This kind of structure would therefore be very well suited for security applications, for example in polymer bank notes. They could complement the existing reflection-based holograms by adding security features working in transmission to the transparent parts of such banknotes.

Let us finally note that the colors are also similar and well visible under non-polarized illumination, although they are less saturated due to the addition of mostly uncolored TM-polarized light.

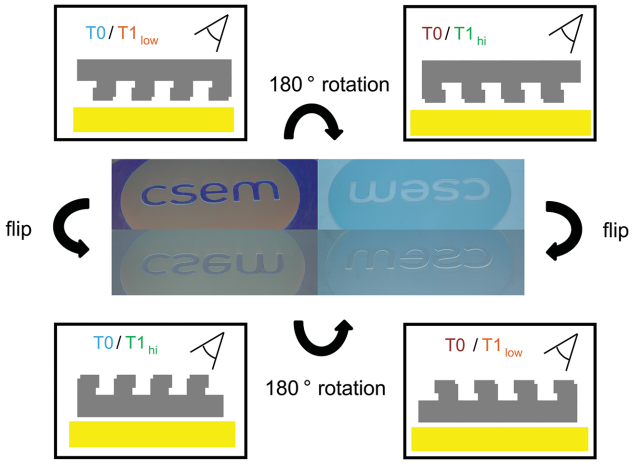

Figure 6. TE-polarized photographs of a sample containing a 440-nm (letters) and a 350-nm period grating (surrounding circle) shown together with sketches illustrating the orientation at which they were recorded. By flipping or rotating the sample, different mixtures of zero ($T0$ at $\pm\theta_i$) and higher transmission orders ($T_{hi/low}$) could be obtained.

2.3. Floating Screen Films

Until now, only gratings in close contact with the light source have been considered, which led to a mixing of $T0$ and $T\pm1$. By moving the grating far enough away from the light source, the directly transmitted rays can be separated from the diffracted ones, as depicted in **Figure 7**a and b. A duplicate of the image will then appear at the position of the grating surface and the directly transmitted picture will stay visible at the old position. By choosing a flexible substrate for the grating, for instance polycarbonate, it is also possible to create curved floating screen films, Figure 7c–e. The use of such a substrate also nicely evidences the transition from the mixing regime to the floating screen regime, which corresponds to the continuous change from the letter "c" to the letter "m" in the photos in Figure 7. It is important to mention that the structure needs to be oriented such that $T1_{hi}$ is diffracted towards the observer. Figure 7 illustrates the two appropriate orientations: in panel (a) the grating faces the observer, which shows stronger colors; whereas in panel (b) the grating is on the side of the light source, leading to a higher overall transmittance. This difference is very well demonstrated by comparing the photos taken in configuration (a) (Figure 7c) to the one taken in configuration (b) (Figure 7d), where a commercial smart phone displaying a white CSEM

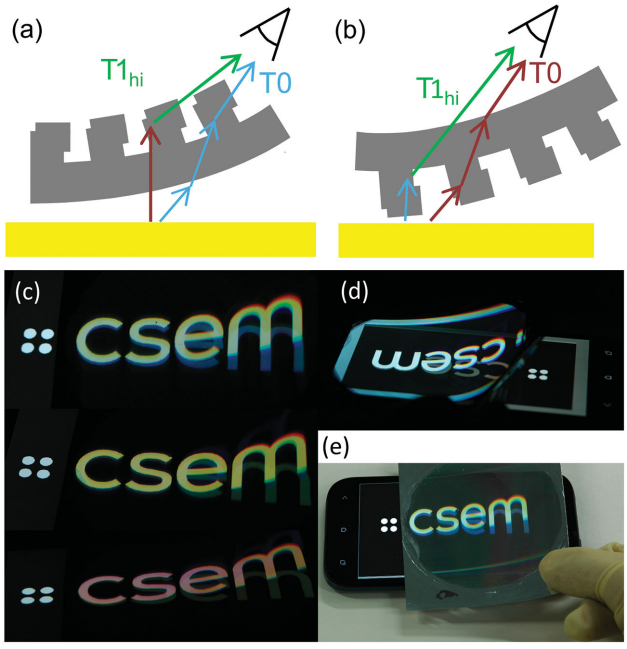

Figure 7. Sketches illustrating how the structure acts as a floating screen film in the case of a) $\theta < 0$ and b) $\theta > 0$. c,e) Photographs taken in configuration (a) at different angles and d) photographs for configuration (b). e) Actual setup used for taking all of the photos, which proves that the floating screen film is even operational in ambient light. The sample used is a hot embossed, flexible Polycarbonate grating of 560 nm period, evaporated with Al at $\alpha > 45°$.

logo was used and the four dots were left uncovered in all photos for comparison. The colors were even partially tunable by adjusting the angle of view, as illustrated by the three pictures in Figure 7c. The grating or evaporation parameters can also easily be adapted to generate a variety of color combinations. Finally, the color of both images is strong enough to even be visible in ambient light (Figure 7e), only the reflected orders may disturb the visibility. By choosing a stronger light source than the mobile phone used for Figure 7, the visibility of the two images can also be further improved. Under dimmed illumination, reflections are excluded and the colored shapes are always perfectly visible.

An application of this could be brand protection or decoration of mobile phones. As the light emitting layer of mobile phones is already covered by a pane of a certain thickness, only a small additional spacing would be required in order to enable a floating screen film. It would therefore be possible to incorporate the structure into the device wrapping (when sealing it at the factory) or mount it in on a showcase (e.g., for presentation in a store). Another convenient property of many mobile phones is that they already emit partially polarized light (LCD displays are the most common technology), which enhances the visual effect through the use of mainly TE-polarized light. Effects similar to those presented in this article have to our knowledge not been demonstrated before. They are also easy to recognize and rely on a different fabrication method than state-of-the-art holograms. These properties are favorable for customer recognition, but also for preventing counterfeits: Consumers can often not distinguish between a complex, genuine hologram and a much simpler imitation with a comparable holographic effect. The properties described here are very different from these holograms, which requires forgers to reproduce the reported structure and hence invest much more money and work in order to deceive customers.

3. Conclusion

We have presented a new way of generating color effects using angle evaporation of metals at a dielectric grating. Although the fabrication procedure has already been used for more than thirty years, to the best of our knowledge it had not been used before for the generation of color effects through $\pm 1^{st}$ diffraction orders. We demonstrated several possibilities of doing so, ranging from asymmetric color effects to floating screen films. Applications of these optical effects include security or decorative features for light-emitting devices, such as mobile phones, or bank notes for instance. This approach is easy for mass production, as the entire fabrication can be performed in a roll-to-roll process. Even the generation of asymmetrically visible images can be performed in a two-step process consisting of one imprint step and one angle-evaporation step.

4. Experimental Section

Fabrication: The fabrication procedure is illustrated in Figure 2. UV-curable Ormocer was cast from a holographically originated (see Niederer et al.[35]), electroplated nickel master grating with a subwavelength period, Figure 2a. In the case of patterned gratings, a printed shadow mask was applied for the replication of a second grating on top of the first one. Subsequently, aluminum was evaporated on the grating at an angle $\alpha > 60°$ with respect to the surface normal using a Balzers BAK 550 coating system, Figure 2b. The shape of the coating can be tuned by varying the evaporation angle or the distance between sample and source. A SEM image of the resulting asymmetric, shadow-evaporated structure is shown in Figure 2c. Polycarbonate was hot embossed with a HEX 01 system and evaporated in the same manner. Zero-order transmittances (T0) were measured between $\theta_i = -60°$ and 60° using a Perkin Elmer Lambda 9 spectrophotometer.

Simulations: A sketch of the model used for simulations is displayed in Figure 2d, together with the definitions of the different parameters. Figure 2b shows the definition of polarizations for a grating in classical mounting (the plane of incidence is perpendicular to the grating lines).

Simulations were performed with rigorous coupled-wave analysis (RCWA)[36] based methods using the model shown in Figure 2d. A constant refractive index of 1.5 was assumed for the UV-curable polymer, the refractive index for Al was taken from Rakic.[37] The design parameters for the structure were the grating depth t, the period Λ, the structure width w, the evaporation angle α with respect to the surface normal, and the evaporated metal thickness D (as set on the evaporator). The metal thicknesses on the top (h) and on the sidewall of the grating (d), as shown in Figure 2d, are related to D and α, respectively, through simple geometrical considerations: $d = D\sin(\alpha)$ and $h = D\cos(\alpha)$. Also, the metallization depth s on the sidewall of the grating is determined by the width w of the grating lines, the period Λ, and the evaporation angle α using the relation $s = (\Lambda - w)/\tan(\alpha)$. A similar geometrical approach was also used by Ye et al., although they did not correct the metal thicknesses for the evaporation angle in their work.[23] A final feature visible in the SEM images is a small uncovered part on the top of the grating. The corresponding dimension is set to $0.03 * \Lambda$, which is consistent with the SEM images. The width w was measured to be $0.03 * \Lambda$, corresponding to a duty cycle of 0.3.

The conversion of spectra into XYZ and RGB color values was performed using the Spectral Color Matlab toolbox available from the University of Eastern Finland.[38] The D65 daylight spectrum was chosen as the light source and CIE 1931 tri-stimulus values were used for the color perception. The corresponding RGB and XYZ values could then be used for the Matlab plots. A modified version of the toolbox accompanying S. Westland's book was used to create the chromaticity diagrams.[39]

Supporting Information

Supporting Information is available from the Wiley Online Library or from the author.

Received: June 3, 2015
Revised: July 29, 2015
Published online:

[1] P. Vukusic, J. R. Sambles, *Nature* **2003**, *424*, 852.
[2] S. Kinoshita, S. Yoshioka, J. Miyazaki, *Rep. Prog. Phys.* **2008**, *71*, 076401.
[3] O. Sato, S. Kubo, Z.-Z. Gu, *Acc. Chem. Res.* **2009**, *42*, 1.
[4] T.-S. Wong, S. H. Kang, S. K. Y. Tang, E. J. Smythe, B. D. Hatton, A. Grinthal, J. Aizenberg, *Nature* **2011**, *477*, 443.
[5] W. Barthlott, C. Neinhuis, *Planta* **1997**, *202*, 1.
[6] J. Teyssier, S. V. Saenko, D. van der Marel, M. C. Milinkovitch, *Nat. Commun.* **2015**, DOI: 10.1038/ncomms7368.
[7] K. Watanabe, T. Hoshino, K. Kanda, Y. Haruyama, S. Matsui, *Jpn. J. Appl. Phys. Part 2-Lett. Express Lett.* **2005**, *44*, L48.

[8] C. Lawrence, P. Vukusic, R. Sambles, *Appl. Opt.* **2002**, *41*, 437.
[9] P. Nussbaum, I. Philipoussis, A. Husser, H. P. Herzig, *Opt. Eng.* **1998**, *37*, 1804.
[10] H. Giessen, *Nat. Photonics* **2008**, *2*, 335.
[11] M. Gale, K. Knop, R. Morf, *Proc. SPIE 1210* **1990**, *1210*, 83.
[12] K. Kumar, H. Duan, R. S. Hegde, S. C. W. Koh, J. N. Wei, J. K. W. Yang, *Nat. Nanotechnol.* **2012**, *7*, 557.
[13] S. J. Tan, L. Zhang, D. Zhu, X. M. Goh, Y. M. Wang, K. Kumar, C.-W. Qiu, J. K. W. Yang, *Nano Lett.* **2014**, *14*, 4023.
[14] T. W. Ebbesen, H. J. Lezec, H. F. Ghaemi, T. Thio, P. A. Wolff, *Nature* **1998**, *391*, 667.
[15] J. A. Porto, F. J. Garcia-Vidal, J. B. Pendry, *Phys. Rev. Lett.* **1999**, *83*, 2845.
[16] Q. Cao, P. Lalanne, *Phys. Rev. Lett.* **2002**, *88*, 057403.
[17] F. J. Garcia-Vidal, L. Martin-Moreno, T. W. Ebbesen, L. Kuipers, *Rev. Mod. Phys.* **2010**, *82*, 729.
[18] T. Xu, Y.-K. Wu, X. Luo, L. J. Guo, *Nat. Commun.* **2010**, *1*, 59.
[19] P. Schau, K. Frenner, L. Fu, H. Schweizer, H. Giessen, W. Osten, *Opt. Express* **2011**, *19*, 3627.
[20] P. Lalanne, J. P. Hugonin, J. C. Rodier, *J. Opt. Soc. Am. A* **2006**, *23*, 1608.
[21] J. Sauvage-Vincent, Y. Jourlin, S. Tonchev, C. Veillas, P. Claude, O. Parriaux, *Proc. SPIE 8428* **2012**, *8428*, 84280F.
[22] H. Lochbihler, *Opt. Express* **2009**, *17*, 12189.
[23] Y. Ye, R. Shao, Y. Zhou, L. Chen, *Appl. Opt.* **2012**, *51*, 5785.
[24] H. Lochbihler, *Phys. Rev. B* **2009**, *79*, 245427.
[25] L. Zhu, J. Kapraun, J. Ferrara, C. J. Chang-Hasnain, *Optica* **2015**, *2*, 255.
[26] M. Aschwanden, A. Stemmer, *Opt. Lett.* **2006**, *31*, 2610.
[27] S. Astilean, P. Lalanne, P. Chavel, E. Cambril, H. Launois, *Opt. Lett.* **1998**, *23*, 552.
[28] T. Levola, P. Laakkonen, *Opt. Express* **2007**, *15*, 2067.
[29] A. Baron, E. Devaux, J.-C. Rodier, J.-P. Hugonin, E. Rousseau, C. Genet, T. W. Ebbesen, P. Lalanne, *Nano Lett.* **2011**, *11*, 4207.
[30] C. Palmer, E. Loewen, *Diffraction Grating Handbook*, Newport Corporation, Rochester, NJ **2005**.
[31] F. Lütolf, M. Stalder, O. J. F. Martin, *Opt. Lett.* **2014**, *39*, 6557.
[32] D. Crouse, P. Keshavareddy, *Opt. Express* **2007**, *15*, 1415.
[33] Y. Shen, V. Rinnerbauer, I. Wang, V. Stelmakh, J. D. Joannopoulos, M. Soljačić, *ACS Photonics* **2015**, *2*, 27.
[34] B. Michaelis, D. R. E. Snoswell, N. A. W. Bell, P. Spahn, G. P. Hellmann, C. E. Finlayson, J. J. Baumberg, *Adv. Eng. Mater.* **2013**, *15*, 948.
[35] G. Niederer, H. P. Herzig, J. Shamir, H. Thiele, M. Schnieper, C. Zschokke, *Appl. Opt.* **2004**, *43*, 1683.
[36] M. G. Moharam, T. K. Gaylord, *J. Opt. Soc. Am.* **1981**, *71*, 811.
[37] A. Rakic, *Appl. Opt.* **1995**, *34*, 4755.
[38] University of Eastern Finland Spectral Color Research Group, Spectral Database, https: //www.uef.fi/fi/spectral/spectral-database, accessed: January **2014**.
[39] S. Westland, C. Ripamonti, *Computational Color Science Using MATLAB*, J. Wiley, Hoboken, NJ **2004**.